Non-linear optics for an online probing of the specific surface area of nanoparticles in the aerosol phase

M. Joret, S. Idlahcen, M. Mazur, Jerôme Yon

Journal of Aerosol Science 183 (2025) 106484

Contents lists available at ScienceDirect

Journal of Aerosol Science

journal homepage: www.elsevier.com/locate/jaerosci

Non-linear optics for an online probing of the specific surface area of nanoparticles in the aerosol phase

M. Joret, S. Idlahcen, M. Mazur *, J. Yon

INSA Rouen Normandie, Univ Rouen Normandie, CNRS Normandie Univ, CORIA UMR 6614, F-76800, Saint-Etienne du Rouvray, France

ARTICLE INFO

Editor: Dr. Chris Hogan

Keywords:
Black carbon
Second harmonic generation (SHG)
Hyper Rayleigh Scattering (HRS)
Non-linear optics
Specific surface area

ABSTRACT

In the present study the generation of non-linear optical (NLO) effects, such as second harmonic generation (SHG), by black carbon particles, also named soot, and by other types of nanoparticles in aerosol phase is quantified and analysed. Its potential for measuring the specific surface area of an aerosol is put forward. SHG is a Non Linear Optical phenomenon that is typically used in biosciences and fundamental physics and has shown to have large potential for the investigation of surface sensitive phenomena. It exists in two forms, coherent SHG and incoherent SHG, also named Hyper Rayleigh Scattering (HRS). While applications on particles in solution or organic molecules located on the surface of droplets exist, the SHG naturally induced by solid nanoparticles in aerosol phase without any SHG enhancing additive has neither been detected nor quantified yet. The present work aims at narrowing this gap by exposing a jet of well-characterized nanoaerosols to a femtosecond laser featuring high peak pulse energies allowing to induce NLO phenomena. The experiments are carried out in an innovative optical setup allowing to analyse the NLO response resolved in time, wavelength and angle, thus having the capability to isolate SHG from other phenomena, such as laser filamentation. The optical setup was calibrated in order to quantify the generated signal power and optimized in order to have a high sensitivity and in order to avoid NLO generation from its own optical elements. The results confirm that soot particles, as well as DEHS droplets and arc generated carbon nanoparticles, feature SHG at intensities that are more than 7 orders of magnitude smaller than that of static light scattering. SHG depends in particular on aggregate and/or monomer size. On the other hand, SHG induced by soot does not seem to depend on the organic or elementary carbon content. The experiments also show that the detected NLO signal increases linearly with particle surface area, independently of the particle shape or composition. Finally, the angular response of NLO signal is fundamentally different from that of linear scattering. Due to the isotropic nature of the angular response, the observed SHG signal is probably non-coherent and thus related to Hyper Raleigh Scattering. These findings show the potential of non-linear optics, in particular to quantify in situ the specific surface of an aerosol. Giving access to this information which is crucial in the evaluation of toxicity of aerosols, the present work can thus give way to a new class of laser based diagnostics for aerosols.

1. Introduction

Aerosols of nanoparticles are found in a large variety of natural and human-made processes and act harmfully on the human respirational and cardiovascular health, causing oxidative stresses or inflammatory responses of the human cells which are exposed

* Corresponding author.
E-mail address: marek.mazur@coria.fr (M. Mazur).

https://doi.org/10.1016/j.jaerosci.2024.106484
Received 15 July 2024; Received in revised form 14 October 2024; Accepted 22 October 2024

Available online 2 November 2024

to them (Hill et al., 2023; Jacobson, 2010). These particles also react with molecules in the atmosphere and influence heat transfers, contributing to air pollution and global warming (Bond et al., 2013; Highwood & Kinnersley, 2006). An example for human-made particles is black carbon (BC - or soot in the combustion field) formed during the incomplete combustion of hydrocarbons, for example in aircraft or car engines, industrial plants and fires. Their experimental in-situ analysis is crucial, either at the source to find ways to reduce their production, in diluted media, as the atmosphere, to study their impact, or to validate theoretical models (formation, aging processes, climate impact, ...).

Such experiments are however challenging due to the BC particles' complexity and changes during their formation and aging processes. Also, the impact of these particles depends on their structure and composition, with large quantities of organic compounds, as polycyclic aromatic hydrocarbons (PAH), being particularly dangerous and a high specific surface of the BC aggregate allowing for high reaction rates between PAH and human cells (Bond et al., 2013; Highwood & Kinnersley, 2006; Hill et al., 2023; Jacobson, 2010). BC is formed from combustion radicals connecting to PAH, then to primary spheres and finally to aggregates (Michelsen, 2017). A primary sphere itself consists of different elements which are crystalline, amorph or organic (Bescond et al., 2016) and whose repartition depends on the particle generation history. After emission, the ongoing aging process caused by soot interaction with atmospheric compounds also affects their physical and chemical properties. These can be analysed in-situ with various already existing diagnostics relying on their optical properties. Laser induced incandescence (LII) and light scattering are used in-situ to measure their volume fraction, size and morphology. Particle structure (i.e. whether the particles are of amorphous, graphitic or organic nature) and morphology can also be studied ex-situ by probing and transmission electron microscopy (TEM) or Raman analysis (Bouvier et al., 2019; Ess et al., 2016; Michelsen et al., 2015; Ouf et al., 2016).

However, none of the previously mentioned in situ techniques provide information about the particles' internal structure — this information, such as the quantity of PAH or the specific particle surface (defined as the total surface by mass of particles), would however help to gain insight on particle toxicity. These techniques moreover do not give access to surface-specific phenomena, which would be extremely interesting for the understanding of particle growth/oxidation phenomena as well as the evaluation of their toxicity, which is directly linked to the particles' specific surface (Al Housseiny et al., 2020).

An access to these measurands could be offered by non-linear optics (NLO), which have not or very rarely been exploited for the characterization of black/brown carbon aerosols, even if NLO based techniques are commonly used in other domains, such as biology (Bancelin et al., 2015; Geiger, 2009; Malcom Brown et al., 2003; Marinescu, 2019; Rice et al., 2008; Stoller et al., 2002; Vielreicher et al., 2013) and chemistry (Paul & Corn, 1997; Zdanowicz et al., 2013, 2014), where solid or liquid probes are analysed by non-linear microscopy.

The physical foundations behind NLO are the following: In general, light interacts with the molecules of a medium, which are excited and themselves emit and scatter light. With common light sources, the molecules' elastic scattering response is linear to the incident electric field and the scattered light has the same wavelength and polarization. The term NLO describes the optical response of a medium exposed to very high laser intensities obtained for example by femtosecond lasers (Boyd, 2008). The intensity of the incident light is so high that the medium's response becomes non-linear, leading to effects like the generation of new wavelengths or polarizations, changes in the refractive index of the medium or various multi-photon phenomena (Aldén et al., 1984; Boyd, 2008). Different NLO effects depend on the medium and its molecular structure (Boyd, 2008), such as second and third harmonic generation (SHG and THG), which are respectively the generation of light at frequencies twice or three times the incident light frequency. While THG can be obtained in all kinds of media, SHG can only be observed in non-centrosymmetric media due to cancellation in symmetric materials.

Due to an arbitrary distribution of the different dipoles in an aerosol, it can be considered as centrosymmetric in its globality, yet multiple studies show that an application of SHG for the analysis of aerosols is possible due to surface-related phenomena at the nano-scale, which lead to local symmetry-breaking. Indeed, the review by Bonacina et al. (2020) states different examples of SHG generated by centrosymmetric materials in the nanoscale, even if their symmetry does in theory not allow for SHG and the phase matching length is small due to their small size. The SHG is explained by local asymmetries (on the surface notably) and strong magnetic field gradients, both due to the small size. Concerning aerosols, Wang et al. (1996) demonstrated SHG by dipoles being placed on centrosymmetric nanoparticles of a size that is non-negligible compared to the wavelength. They explained the generation by the fact that even if the dipoles are arbitrarily distributed, the phase difference between the different dipoles is sufficiently large to avoid a complete SHG cancelling.

In more recent studies, SHG has been detected on particles or droplets in aerosol phase due to the prior addition of different types of molecules (Qian et al., 2019, 2018; Wu et al., 2016). While the first works needed to use specific molecules with strong quadratic hyperpolarizabilities, such as dyes, (Qian et al., 2018; Wu et al., 2016), follow-up studies were used to detect ethanol or different types of acids on the particle surfaces (Qian, Brown, Huang-Fu et al., 2022; Qian, Brown, Zhang et al., 2022). These results could even be extended to Sum frequency generation, an advanced NLO technique allowing to concentrate on specific molecules (Brown et al., 2023; Qian et al., 2020a, 2020b). The importance of the surface interactions between the aerosol and the surrounding medium has been confirmed in multiple different studies including the analysis of lithium niobate particles formed by freezing (Matrokhin et al., 2022), on thin films at nm scale (Das et al., 2021) or in nanocrystalline silicon nanoparticles (Makarov et al., 2017).

Different experimental and theoretical studies have also been carried out on the angular dependence of non-linear scattering in particle at nano and micrometre scales, which are well summarized in Roke and Gonella (2012). In particular de Beer et al. (2011) developed a discrete dipole model of Rayleigh scattering on arbitrarily shaped particles taking into account the non-linear effects leading to phenomena as the scattering of SHG on the particle surface, also named second harmonic scattering (SHS). They analysed the SHG signal in terms of angular dependence and showed that due to the non-linear susceptibility tensor, the scattering of the dipoles is cancelled out in forward direction, thus being zero, contrarily from what is known in linear scattering. These findings

were also confirmed experimentally on testing the angular response of nanoparticles suspended in water (Martinez Tomalino, 2009; Martorell et al., 1997; Schürer et al., 2011). The same group had also investigated the dependence of the SHG signal on monodisperse particle size and concentration and has shown that, for a chosen particle size, the SHG signal depends on the particle concentration following a log-normal trend with a maximal value occurring at higher concentrations for smaller particles (Schneider et al., 2007). Another interesting property is the coherence nature of the SHG. Indeed, as explained in Hollis (1988), Das (2006) and Le Breton (2022), SHG is constituted of a coherent and an incoherent part. The former is due to a direct interaction between the electric field and its harmonic, is associated with a high anisotropy and phase-coupling with the incident light and is happening on the scale of the entire medium. The latter is due to the absorption of two photons and the re-emission of a single photon by separate dipoles in the medium and is associated with isotropic emission. The incoherent SHG is commonly named Hyper Rayleigh Scattering (HRS) in literature.

While the previous studies demonstrated SHG on different type of aerosols that are either homogeneous or have added materials with high SHG on their surface, it has not yet been examined on more complex aggregates with different types of structures (crystalline, amorphous or organic), such as black carbon. Very recently, third-harmonic generation and scattering have been observed on soot particles generated in flames (Zang et al., 2020, 2018). Yet, no attempt has been made to analyse SHG on these particles. Moreover no information is provided about the aerosols' properties (size distribution, morphologies) in these studies.

In the stated context, the present study demonstrates and quantifies for the first time with the help of an innovative experimental setup for the possibility of SHG measurements on different types of nanoparticles in aerosol phase due to an exposition to highly intense femtosecond laser light. The dependence of the SHG signal on the particle size distribution and internal structure are also discussed. Finally the SHG induced by black carbon particles is compared with other femtosecond laser induced phenomena (elastic scattering of the original laser light, laser filamentation) in terms of temporal, spectral and angular response. The findings help to understand the importance of surface related phenomena and give way to new potential class of diagnostics allowing to study surface related phenomena in black carbon particles, especially during their formation and aging in the atmosphere or when analysing their toxicity. Indeed, previous studies have shown the importance of the reaction surface on black carbon nanoparticles' on the particle toxicity (Al Housseiny et al., 2020), and the combination of specific surface area measurement by SHG together with toxicologic measurements as carried out by Juarez-Facio et al. (2022) could be used to directly investigate the link between these two parameters.

2. Methodology

2.1. Particle generation and properties

The non linear optical response of multiple types of carbonaceous nanoparticles in aerosol phase is analysed in the present study, featuring different types of internal structures, different size distributions and particle morphologies.

Three types of aerosol generators are used: A miniCAST 5201c soot generator which generates the particle by burning a fuel-rich mixture of propane, nitrogen and air. The particles properties, such as size distribution and internal structure are altered by varying the different gas flows, resulting in the operating points names CAST1, CAST2 and CAST3, that are known as reference particles in the soot community (Bescond et al., 2014; Ouf et al., 2016) and have different predominant types of structures (crystalline, amorphous or organic), as shown in Table 1. Typical TEM images of the internal structures of these types of soot are shown in Fig. 1a, where one can in particular observe the difference between the highly structured crystalline layers in CAST1 and the non-structured organic content in CAST3, with CAST2 being a point in-between. The second type of generators is a PALAS GfG 1000 which generates amorphous carbon particles by repeated sparks between two graphite electrodes in an Argon flow (Knauer et al., 2009). Fig. 1b shows the internal structure of particles generated by the PALAS device, which can be characterized by the absence of global patterns as seen in the crystalline parts of CAST1 for instance. Except for the PALAS variation study in Section 3.2, the device is kept constantly at 1.5 bar argon pressure and 1000 Hz electric discharge frequency. Finally a TSI atomizer is used to generate spherical DEHS (Di-Ethyl-Hexyl-Sebacate) droplets, which consist of organic carbonaceous chains. The different particles' structural properties are summarized in Table 1.

The choice of different types of CAST particles is motivated by their differences in internal structure and the structures' influence on the particles' chemical properties and toxicity, as shown in the chemical and toxicological study of CAST1 and CAST3 soot in Juarez-Facio et al. (2022). Indeed, that study has shown by mass spectrometry that CAST1 particles feature a high quantity of small PAH compounds, while CAST3 soot consists of larger PAH molecules. Moreover, the exposure of human lung cells shows substantial effects on their gene expression when exposing with CAST3 soot, while no influence is observed with CAST1 soot (Juarez-Facio et al., 2022).

2.2. In-line particle sizing and counting

In order to be able to distinguish between different particle size distributions and in order to normalize the measurement with particle concentrations, a Scanning Mobility Particle Sizer (SMPS) is used in-line for measuring size distribution and concentration, preceded by a VKL particle dilution system in order to avoid the SMPS to saturate. The device is commonly used in aerosol studies (von Bismarck-Osten et al., 2013) and is based on pre-charging of particles and the subsequent measurement of their displacement in an electric field.

Table 1
Summary of the different aerosols that were used in the present study (Bescond, 2015; Ouf et al., 2016).

Caption	Generator	Structural properties
CAST1	miniCAST	Mainly crystalline soot aggregates, 4% organic carbon
CAST2	miniCAST	Intermediate between CAST1 and CAST3
CAST3	miniCAST	Mainly organic soot aggregates (87% organic carbon, the rest is mostly amorphous)
PALAS	PALAS GfG	Amorphous pure carbon aggregates
DEHS	TSI atomizer	Spherical liquid nano-aerosol

Table 2
$\overline{D_p}$, d_f and ρ are respectively the primary sphere size, the fractal dimension and the particle density, found in literature (Bescond, 2015; Ouf et al., 2016). $\overline{N_{tot}}$ is the particle concentration measured by SMPS, as described in Section 2.2. $\overline{D_{m,geo}}$ and $\overline{\sigma_{m,geo}}$ correspond to the log-normal fit parameters based on particle size distribution measurements by SMPS. The remaining parameters are calculated with the help of the analytical model in Yon et al. (2015). $\overline{N_p}$ and $\overline{N_p^2}$ correspond to the mean number of primary spheres per aggregate and the mean of its square. $\overline{f_S}$ and $\overline{f_V}$ are respectively the mean particle surface and volume fraction. $\overline{S_{particle}}$ and $\overline{V_{particle}}$ are respectively the mean surface and volume of one particle. $\overline{SSA}$ is the mean Specific Surface Area defined as $SSA = \overline{S_{particle}}/(\overline{V_{particle}} \cdot \rho)$.

Aerosol	CAST1	CAST2	CAST3	DEHS	PALAS
$\overline{D_p}$ [nm]	29.6	39.1	32.0	–	7.0
d_f	1.73	1.76	1.79	3	1.61
ρ [kg/m^3]	1543	1235	1321	912	2150
$\overline{N_{tot}}$ [#/cm^3]	$4.80 \cdot 10^7$	$2.98 \cdot 10^7$	$7.53 \cdot 10^7$	$2.53 \cdot 10^7$	$6.8 \cdot 10^7$
$\overline{\sigma_{m,geo}}$	1.65	1.59	1.76	1.72	1.63
$\overline{D_{m,geo}}$ [nm]	97	112	56	212	112
$\overline{N_p}$	44	32	14	1	730
$\overline{N_p^2}$	6100	2840	1140	1	$1.1235 \cdot 10^6$
$\overline{f_S}$ [m^2/m^3]	5.79	4.52	3.41	3.57	7.65
$\overline{f_V}$ [ppb]	28.55	29.49	18.18	125.79	8.92
$\overline{S_{particle}}$ [nm^2]	$1.21 \cdot 10^5$	$1.52 \cdot 10^5$	$4.53 \cdot 10^4$	$2.45 \cdot 10^5$	$1.12 \cdot 10^5$
$\overline{V_{particle}}$ [nm^3]	$5.95 \cdot 10^5$	$9.98 \cdot 10^5$	$2.41 \cdot 10^5$	$1.68 \cdot 10^7$	$1.31 \cdot 10^5$
$\overline{SSA}$ [m^2/g]	131.4	124.3	142.1	31.1	398.7

2.3. Optical signal generation and detection setup

The optical setup is presented in Figs. 2 and 3. It aims at focusing the high intensity laser beam in the measurement volume and collecting the SHG and other signals resulting from the laser/particles interaction in an angularly, spectrally and temporally resolved way. The setup is motivated by multiple theoretical and experimental studies that have demonstrated an angular dependence of SHG (Gonella & Dai, 2014; Wunderlich et al., 2012) as well as an angular and spectral dependence of other femtosecond laser induced phenomena, such as laser filamentation (Durand, 2011).

The used laser source is a Coherent Libra II femtosecond laser, producing a 800 nm linearly (vertical to the laboratory reference frame) polarized light with a pulse duration of 100 fs, at a frequency of 1 kHz and a maximum energy of 3.5 mJ. In order to ensure a stable laser power, the laser is set to its standard working current of 20 A, generating around 1 W of average power. The beam traverses a Half wave plate and polarizer assembly (HW1 & Pola1), in which the half wave plate is rotated to fine-tune the incident laser power on the sample in order to avoid significant ionization in the interaction region. A filter of 800 nm central wavelength and 12 nm spectral width ensures that no SHG results from the light–matter interaction in the half wave plates, as observed in Clark et al. (2014). The beam is then focused by a convex lens of 300 mm focal length into a region of a jet of generated particles, as shown in Fig. 4. The different mirrors are ultrafast dielectric mirrors, in order to avoid a spectral broadening of the laser beam.

With a maximum laser pulse energy of 1 mJ (corresponding to the maximum power of 1 W), the laser intensity has a value of around $8 \cdot 10^{12}$ W/cm^2. While this value is extremely high, the time scales leading to phenomena as laser-induced breakdown or incandescence are several orders of magnitude slower that the one required to generate NLO effects (Son & Tereshonok, 2010).

Two detection setups are used in order to obtain different types of information. Fig. 2 shows the detection that is carried out by two custom built Hamamatsu multianode High Sensitive compact Spectrometers (HSS), alternately used for the UV (H10515B-103 with 16 channels ranging from 192.9 to 412.4 nm) and visible range (H7260-20 with 32 channels ranging from 388.2 to 810.2 nm), with a fibred end that is mounted on a motor controlled rotation system. The detectors themselves are multianode multiplier tubes, which are characterized by their high signal sensitivity. The signals are treated by a Vertilon IQSP480 PhotonIQ 32-channel data acquisition system. The spectrometers offer the possibility of angularly resolved measurements with a good temporal description of the signals in a wavelength range between 200 nm and 800 nm. The fibre can be switched to a Princeten Instruments ICCD spectrometer which is used to validate the HSS spectra. Due to mechanical limitations of the setup, there is no access to the transmission measurement at zero degrees.

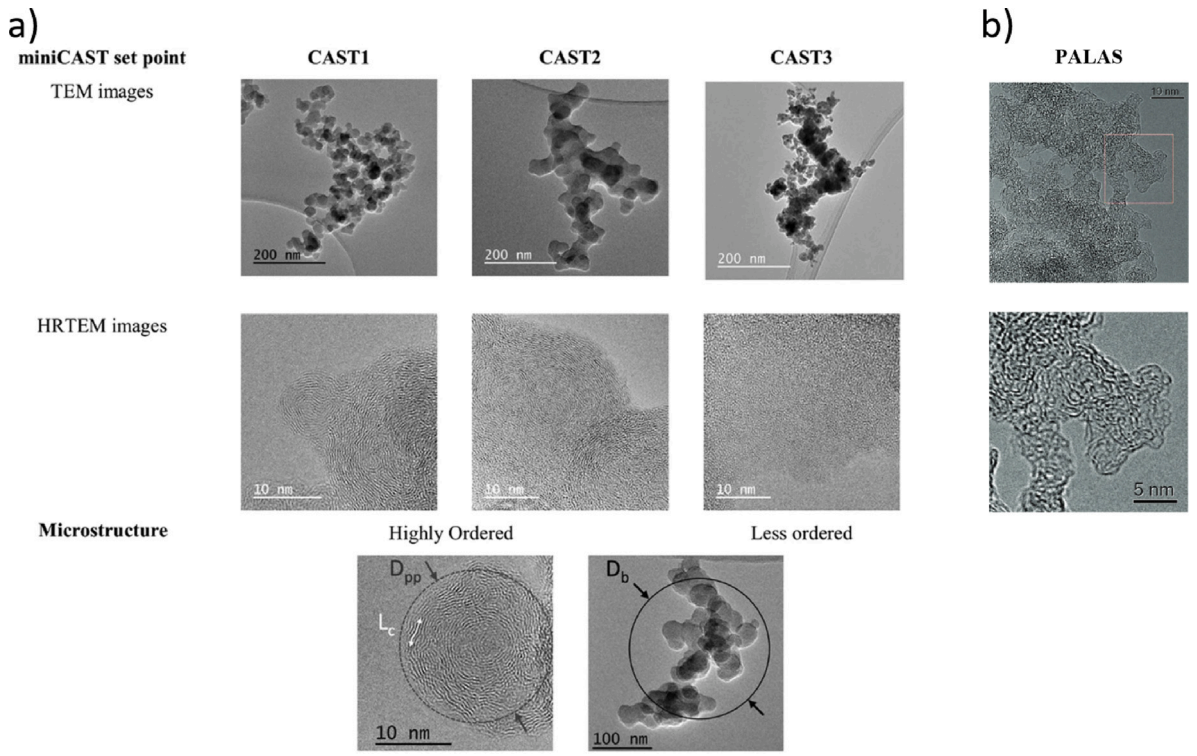

Fig. 1. TEM images of soot particles produced a miniCAST generator for the setpoints (a) CAST1, CAST2 and CAST3 (Ouf et al., 2016) and (b) PALAS GfG (Knauer et al., 2009). The crystallites length (Lc), the primary particle diameter (Dpp) and the electrical mobility diameter (Db) of a soot aggregate are shown at the bottom of the figure.

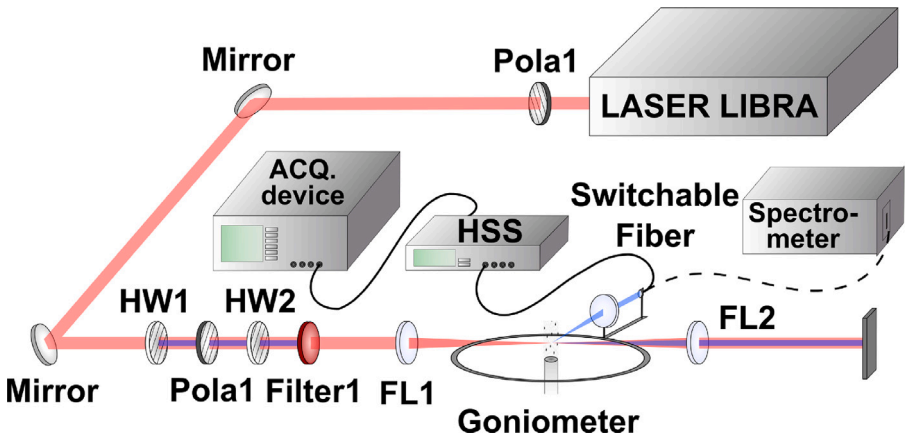

Fig. 2. Optical setup using a high sensitivity spectrometer (HSS) as a detection. HW: Half-wave plate, FL: Focusing lens, Pola: Polarizer, DM: Dichroic mirror, ACQ: Acquisition.

In the setup presented in Fig. 3, the fibre head is connected to a Hamamatsu - H3378-50 photomultiplier, which features a faster time response (in the order of a few ns). An 800 nm IR-blocking filter as well as a filter of either 400 nm or 532 nm is mounted, allowing to obtain quantitative data on SHG and other filament induced phenomena. In parallel, a compact Maya spectrometer is installed at 35 degrees (at the other side of the optical path relative to the rotating detection) and centred at 800 nm with the aim to measure an elastic scattering reference signal.

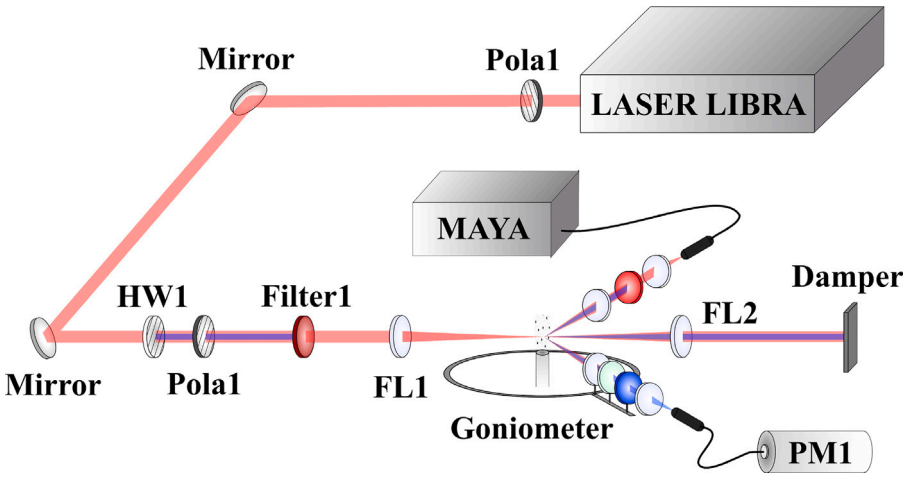

Fig. 3. Optical setup using a photomultiplier (PM) tube as a detection. HW: Half-wave plate, FL: Focusing lens, Pola: Polarizer, DM: Dichroic mirror.

2.4. Signal calibration

The calibration of the measured signals is carried out with a Labsphere CA-13773-UJF integrating sphere. It is constituted by a halogen lamp that is placed inside a closed sphere, walls that act as a black body at variable temperatures for a wide spectral range and an outlet hole for the light. The outcoming light is transported with an optical fibre to a spectrometer that was calibrated by NIST. The integrating sphere is thus a light source with well defined absolute radiance for the spectral range of interest. It is installed in front of the different detection systems presented in Section 2.3, and thus at the location where the laser is focused afterwards, in order to be consistent with the detection that is calibrated. The measured signal can be transformed into measured powers with the equations presented in Appendix A in the annex.

3. Results and discussion

The present section presents the results obtained by the optical setup depicted in Figs. 2 and 3, which have the aim to demonstrate the existence of SHG/HRS due to the interaction of femtosecond laser light at 800 nm with different types of nanoparticles in aerosol phase and to investigate its dependence on different parameters. The different types of particles are presented in Section 2.1 and are black carbon (CAST1), brown carbon (CAST3) and intermediate soot (CAST2), DEHS ($C_{26}H_{50}O_4$) droplets and arc generated carbon nanoparticles (PALAS).

A photograph of interaction between the particles and the femtosecond laser light focused on the nozzle exit is shown in Fig. 4. A sharp bright light blue line along the laser axis is well visible, corresponding to the filamentation of the laser light in the aerosol, a third order NLO effect, where the high energy of the light leads to a virtual modification of the optical index (Kerr-effect) and to focusing of the light. With increasing focus, the local energy is increasing, thus generating a plasma with consequent local ionization and generation of a plasma. The ionization itself defocuses the beam. The sequence between focalization and defocalisation is repeated over a certain distance. The filamentation can already be seen at low laser energies, only during the presence of aerosols. Due to the different time scales between NLO effects, such as SHG and HRS, and the creation of the plasma, the plasma itself does probably not have an influence on the measured results, as will be discussed at a later point in this article.

A more detailed explanation of laser filamentation can be found in Durand (2011) and while it is the explanation for some of the observations, it is not the focus of the present study. Nevertheless, the light blue (almost white) colour of the filaments indicate the broadband nature of the light–particle interactions.

3.1. SHG/HRS validation and quantification

More insight on the spectral response of the light particle interaction can be seen in Fig. 5, at 1 W laser power, collected at 35 degrees as described in Section 2.3. The figure features measurements by the high sensitivity spectrometer (HSS — columns in the figure) as well as a reference ICCD spectrometer (solid line). The spectral response of the measurement is very rich, in particular in the range from 350 nm to 650 nm. One can observe in this zone a large broad band contribution and a strong peak at 400 nm. A notable signal can be seen at 800 nm, while no signal can be observed in the UV region below 350 nm. The spectral richness of the signal can be explained by laser filamentation, which is known to be a broad-band phenomenon (Boyd, 2008; Durand, 2011). The 400 nm peak is associated with incoherent SHG (which is also named HRS in literature), as will be demonstrated in the remainder of the study, while the peak at 800 nm are remainders of the strongly filtered linearly scattered 800 nm laser light. The absence of a signal below 350 nm, and in particular the absence of a peak around 266 nm shows that no THG can be detected in the present

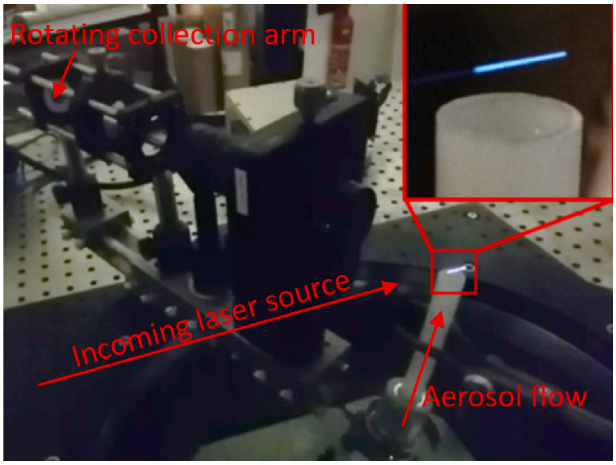

Fig. 4. Photograph of interaction between particle jet coming out of the white nozzle and femtosecond laser (800 nm) focused on the nozzle exit. One can see a strong laser filament.

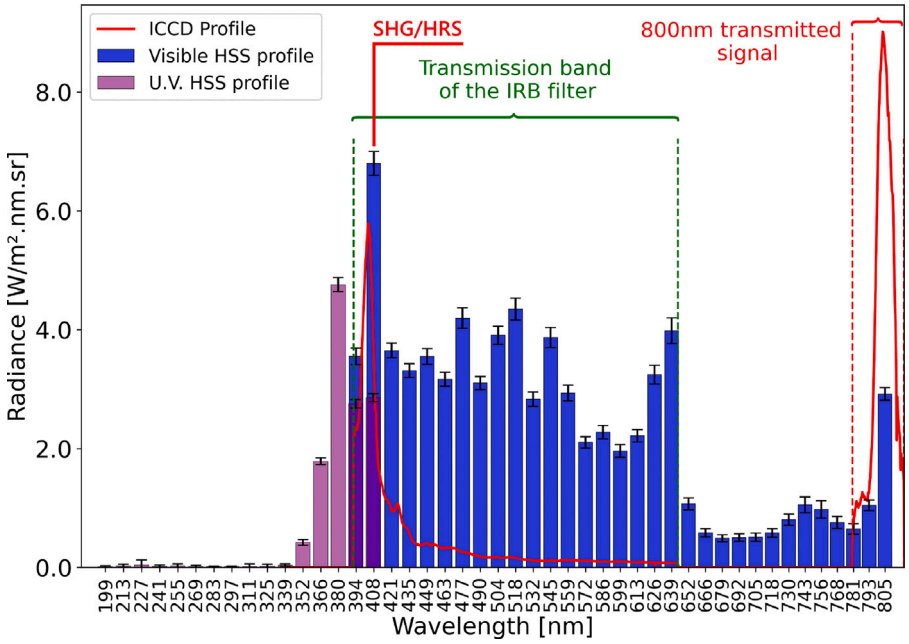

Fig. 5. NLO spectrum of CAST1 particles at 35 degrees and 1 W laser power taken by the HSS spectrometer (columns) and a reference ICCD spectrometer (solid line). The different wavelengths in the horizontal axis correspond to the centre wavelength of each channel of the HSS. (For interpretation of the references to colour in this figure legend, the reader is referred to the web version of this article.)

experiment, contrarily to the findings in Zang et al. (2018), which can be either due to the fact that the signal does not exist or that its amplitude is too low to be detected by the present system. The remainder of the study will mainly concentrate on the detected SHG/HRS signal at 400 nm.

More evidence for the existence of SHG/HRS is given when analysing the dependence of the NLO response on the laser power by using the setup shown in Fig. 3. Fig. 6 compares the response of CAST1 particles at 35 degree detection angle for SHG/HRS (400 nm), linear scattering (800 nm) and the non-linear broadband effects (532 nm). One can see that while the 800 and 532 nm response are close to linear (at least for pulse energies below 0.6 mJ), as expected, the 400 nm response features two regimes: a low-power regime, where the NLO response is quadratic, as shown by the fit in the figure, as well a saturation regime, where the dependence becomes linear and decreases with laser power. The cutoff between the two regimes is found to be at 0.59 mJ pulse energy for this aerosol. The 532 nm and 800 nm signals also have a slight change of slope at that energy, certainly related to the presence of filamentation, however they maintain their close to linear nature. The observed signals are very short, with a rise time of below 1 ns and a decay time of around 10 ns (not presented here), which both correspond to the characteristic times of the PM

Table 3
Fit coefficients, as shown in figure 6, for the different aerosols and cut-off pulse energy from figure 7.

Aerosol	A (W/sr nm mJ^2)	B (W/sr nm mJ)	C (W/sr nm)	Cut-off pulse energy (μJ)
CAST1	0.0759	−0.01189	0.03292	588
CAST2	0.1026	−0.00055	0.03125	549
CAST3	0.0520	0.00348	0.01446	562
PALAS	0.0824	−0.00634	0.04334	688
DEHS	0.0138	0.01075	−0.00094	680

detector. The phenomena are thus shorter, which corresponds to the fact that NLO effects are instantaneous. The quadratic response in the low power regime is typical for SHG/HRS, where as a second order NLO phenomenon the response is supposed to be quadratic to the input laser power (Boyd, 2008). The measurement is thus a proof that the observed 400 nm signal is indeed SHG or HRS. Furthermore, since the measurements have been calibrated with the help of an integrating sphere as described in Section 2.4, the SHG/HRS signal can be quantified, which, to the authors' knowledge, is the first time for aerosol induced SHG/HRS. The measured power is described by Eq. (A.10), which includes the signal calibration and which is developed in the annex, and is around more than 7 orders of magnitude smaller than linear scattering. The figure also includes error bars for the SHG measurement, corresponding to the 95% confidence interval. The interval corresponds to up to ± 10 % of the measurements.

The SHG/HRS responses of the different aerosols are compared in Fig. 7. It can be seen that all the tested aerosols feature a low energy regime with SHG typical quadratic relation between detected energy and laser pulse energy as well as a linear saturation regime. In turn, the cutoff between the two regimes is found to vary according to the aerosol and is located between 0.5 mJ and 0.7 mJ par pulse. The maximum intensity is highest for DEHS and lowest (by a factor of around 8) for PALAS soot, with the CAST soot maximum values being located in-between. It is also interesting to note that the slope in the saturated regime is also different for the different aerosols and is found to be positive for PALAS and negative for the other types of particles. The fit coefficients of the different aerosols are summarized in Table 3.

This comparison allows to conclude that SHG/HRS is observed for all tested types of aerosol. Indeed, the spectral analysis has shown a strong peak at 400 nm, thus half the laser wavelength, attributed to SHG/HRS due to its specific quadratic dependency. These two elements thus confirm for the first time the existence of SHG/HRS in black carbon aerosols. No explanation was found for the saturation regime, but possible reasons could be the filamentation or possibly a partial sublimation of the particles. It has also to be noted that the measurements are very sensitive to the optical alignment and also change with the number concentration of the particles.

Based on the results shown in the Figs. 5, 6 and 7 it can be deduced that the plasma, while possibly inducing rapid phenomena in the time scales of the laser pulse, as explained in von der Linde et al. (1997), is not the source of the here observed 400 nm signal.

Indeed, when comparing the calibration spectrum obtained from the HSS (even if spectrally very badly resolved) and the ICCD spectrum, both shown in Fig. 5, to previous work having performed laser induced breakdown spectroscopy LIBS (Delgado et al., 2022; Wan et al., 2021) on organic/carbonaceous aerosols, the same following peaks common peaks can be found around the 400 nm region:

- around 390 nm: CN (0,0) band (Delgado et al., 2022)
- around 409 nm: O II band (Wan et al., 2021)
- around 415 to 420 nm: CN (0,1) band (Delgado et al., 2022)
- around 430 nm: CH (0,0) band (Delgado et al., 2022)

Both referenced studies however do not include any peak at explicitly 400 nm that could be related to particles generated from combustion of propane in air (as done in the CAST generator) or pure carbon (as done in the PALAS generator). Also, previous works in plasma studies show that plasma related peaks depend on laser pulse energy either linearly (Sirven et al., 2008) or by a power law to a power slightly above 1 (Cabalín & Laserna, 1998), but not quadratically. This finding corresponds to our observations on for example the 532 nm peak shown in Fig. 7. The here observed 400 nm SHG/HRS peak, on the other hand, shows a quadratic dependence on laser energy. This is also backed by observations made with the HSS where one could see (not shown in the paper), that the 400 nm peak grows following a power between 1 and 2, while all other frequencies, which are probably linked to the plasma, follow a power below 1. With these findings it can be concluded that the peak at 400 nm is indeed associated with SHG or HRS and not to the plasma.

3.2. Dependence on particle size, internal structure and surface

As shown in Tables 1 and 2 and in Fig. 1, which all describe the physical properties of the particles, the studied aerosols have different types of structures, i.e. different proportions of organic content, amorphous and crystalline structures, but also different aggregate size distributions, particle concentrations, monomer sizes and particle surfaces. The remainder of the studies will thus shed light on the effects of the different parameters.

The role played by the aggregate size is analysed with the help of PALAS soot, since it isolates this parameter from others. Indeed, as described in Section 2.1, PALAS soot is generated by periodic high voltage discharges between two carbon electrodes in an argon

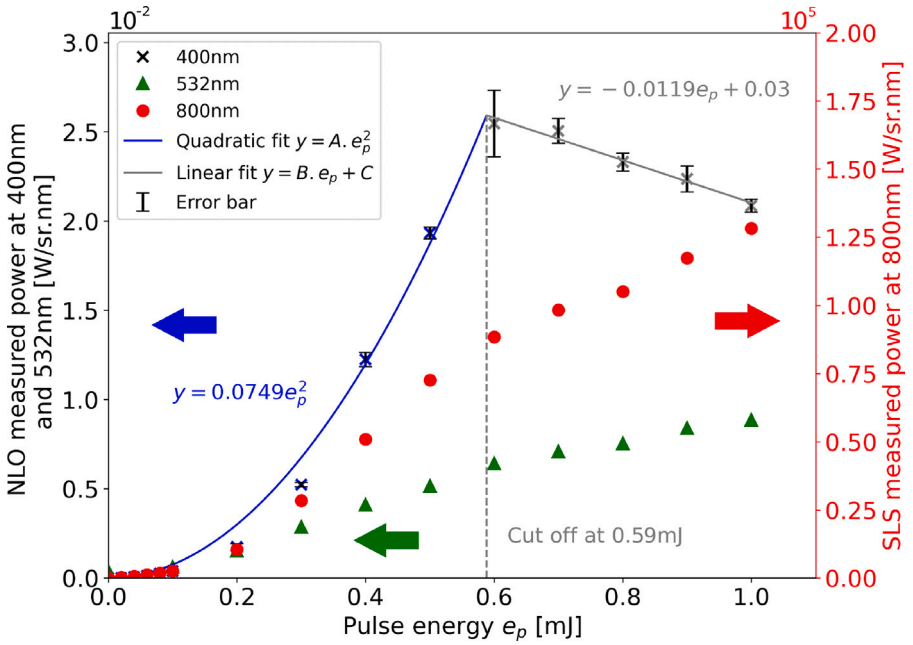

Fig. 6. Linear (800 nm) and non-linear (400 nm and 532 nm) scattering collected at 35 degrees for CAST1 in dependence of the laser power, including a quadratic fit for the low power regime, a linear fit for the saturated regime, the limit between the two regimes and error bars for the non-linear measurement (95 % confidence interval). (For interpretation of the references to colour in this figure legend, the reader is referred to the web version of this article.)

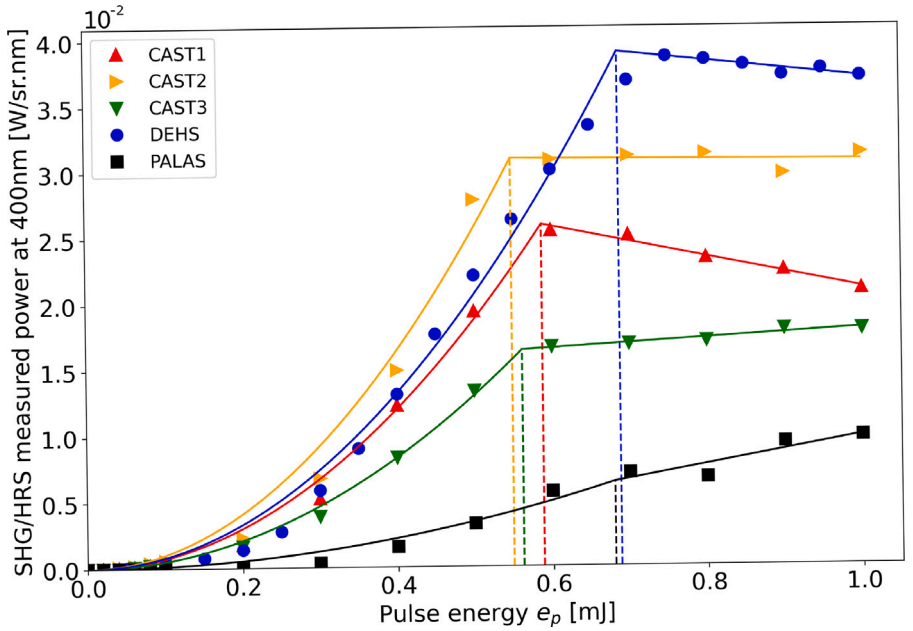

Fig. 7. SHG/HRS fluence curve detected at 35 degrees for the different aerosols, including a quadratic fit for the low power regime, a linear fit for the saturated regime and the limit between the two regimes.

environment. The concentration and aggregate size are varied by changing discharge frequency and argon pressure, while monomer size (7 nm) and particle structure (100% amorphous) remain nearly unchanged. The measurements are normalized by the particle concentration (measured by SMPS, see Section 2.2) in order to isolate the measurements from its effects. The results are presented as a function of $\overline{N_p^2}$, which is the mean of the square of the number of primary spheres per aggregate. $\overline{N_p^2}$ is calculated with the help of the analytical model in Yon et al. (2015), based on the aggregate size measurements by SMPS, combined with the knowledge of

the primary sphere diameter and the fractal dimension, which have both been determined by TEM analysis (Knauer et al., 2009; Ouf et al., 2016). This representation is conform with the scattering description in Sorensen (2001) for static light scattering.

The figure includes the measurement for SHG/HRS as well as for linear scattering and fitting functions of these results. As already confirmed before, the SHG/HRS signal is extremely weak compared to the linear scattering signal. Moreover the dependence on the particle size is different between the two signals. Indeed, the linear scattering signal depends linearly on $\overline{N_p^2}$, as expected in linear scattering theory at small angles, as described in linear scattering studies by the q-region (Sorensen, 2001). The q-region corresponds to an equivalent scattering volume, which decreases in size when the scattering angle increases and in which all elements scatter light in phase. The consequence is that at a small angle, such as 35 degrees in this case, the q-region is larger than the actual aggregate, which is equivalent to the entire aggregate scattering in phase. Therefore, the linear scattering signal at this small angle is proportional to $\overline{N_p^2}$, which is indeed the observation. The SHG signal on the other hand is shown to be proportional to approximately $N_p^{2/3}$. It is important to add that the effects of concentration on the SHG/HRS signal cannot be isolated because all modifications of operating conditions in the particle generator do change both, particle concentration and particle size.

The influence of particle inner structure on SHG/HRS intensity is shown in Fig. 9, depicting the SHG/HRS signal intensity normalized by the particle number concentration for CAST soot with different quantities of oxidation air, thus giving a different organic content, carried out at 35 degrees detection angle and 0.2 mJ per pulse laser energy. The increase of oxidation air flow rate leads to an increase of the elementary carbon to total carbon ratio (EC/TC). The figure also includes the signal for PALAS particles, being 100% amorphous (0% organic) and DEHS being 100% organic. While the organic content is only known for CAST1, CAST2 and CAST3 (Bescond et al., 2016), it is assumed that the CAST points with intermediate oxidation air flow rates in-between will feature organic contents that between the three known points. It can be seen, that both signals, the linear 800 nm signal (SLS — static linear scattering), as well as the non-linear 400 nm signal (SHG/HRS), depend very similarly on the EC/TC ratio, with the maximum being located at around 1.15 Nml/min of air, which corresponds to CAST2. The figure includes a size distribution plot in sub-figure (b), which indicates that CAST2 is also the point with the highest aggregate size. Besides, Table 2 shows that it also features the highest monomer diameter. It can thus be deduced that the amount of elementary or organic carbon does not have a significant influence on the SHG/HRS, which is confirmed by similar measured power for DEHS and PALS, which are respectively fully organic and fully graphitic. Instead, the increase in SHG/HRS seems to be completely related to an increase in aggregate and/or monomer size, as already shown for PALAS particles in Fig. 8.

The findings show that the intensity of SHG/HRS seems to depend more on the particles' dimensions while the particles' internal structure and composition do not seem to have a significant influence. In order to gain a deeper understanding of the driving parameter for SHG/HRS, the measured SHG/HRS signals for the three CAST points, as well as PALAS and DEHS, all normalized by the nanoparticle mass fraction, are plotted against the specific surface area in Fig. 10. The SSA was calculated using the data in Table 2 and gives similar value as found in literature (Ouf et al., 2019). The figure shows that the different measurements align roughly along a straight line, with a slope of $3.53 \cdot 10^{-4}$ W m/sr nm g m^2, independently of the particles' inner structure or morphology. This observation is even more interesting when taking into account the fact that the DEHS particles are particularly large compared to the other studied aerosols, as shown in Table 2. Contrarily, as shown in the volume dependence of SHG/HRS in Fig. B.13, the large volume of the DEHS particles does not lead to a higher SHG/HRS signal compared to the other aerosols. These observations confirm the findings in literature (de Beer et al., 2011; Roke & Gonella, 2012) which indicate that SHG in nanoparticles is generated by symmetry breaking on the surface of the nanoparticles and not at the molecular or atomic level.

3.3. Angular SHG/HRS response

In the present section, the different soot particles are analysed in terms of angular response, an interesting metric for analysing nanoparticle surfaces, as described in multiple studies (de Beer et al., 2011; Martinez Tomalino, 2009; Martorell et al., 1997; Roke & Gonella, 2012; Schürer et al., 2011). The results are shown in Fig. 11, where SHG signal intensity is displayed for CAST1, CAST2 and CAST3, carried out at 0.2 mJ per pulse laser energy. The angle was varied between 35 and 135 degrees, with the range being limited by the mechanical layout of the experimental setup.

The angular SHG/HRS scattering response by particle shows larger SHG/HRS amplitudes toward lower and higher scattering angles, with a minimum value located around 95 degrees scattering angle, for the three tested aerosols. The signal intensity for CAST2 is highest, followed by CAST1 and CAST3, which is linked to the aggregate sizes, as highlighted in the previous section in Fig. 9b. It is interesting to note that the figure seems to be in contradiction to findings in literature (de Beer et al., 2011; Martinez Tomalino, 2009; Martorell et al., 1997; Roke & Gonella, 2012; Schürer et al., 2011), non-linear scattering at zero degrees is supposed to be zero, due to destructive interference associated with the tensor nature of the non-linear susceptibility, however no scattering measurements between 0 and 35 degrees could be made due to geometric limitations of the setup. Another remarkable detail is the fact that the observed scattering profile looks close to function of the type $\frac{1}{sin(\Theta)}$, which corresponds to the variation of the measurement volume due to a rotation of the detection.

Since the scattering of SHG as well as linear scattering are supposed to be associated with the dipoles on the particle surface (de Beer et al., 2011; Roke & Gonella, 2012), it can be interesting to present the angular scattering as a function of the absolute value of the scattering wave vector $\vec{q} = \vec{k_i} - \vec{k_s}$ (with $k_i = 2.pi/\lambda_i$ the length of the incoming light vector and $k_s = 2.pi/\lambda_s$ the length of the scattered linear or nonlinear light vector, (Sorensen, 2001) on a log–log scale, which allows to gain insight on the structure factor, which is used in linear scattering studies for characterizing light-particle interactions. In this presentation, shown in Fig. 12, it is necessary to correct the signals by the measurement volume, which is of the form $sin(\theta)$. As can be seen in the figure, the linear and non-linear signal feature a fundamentally different dependence on q. Indeed, the linear scattering signal is decreasing, probably

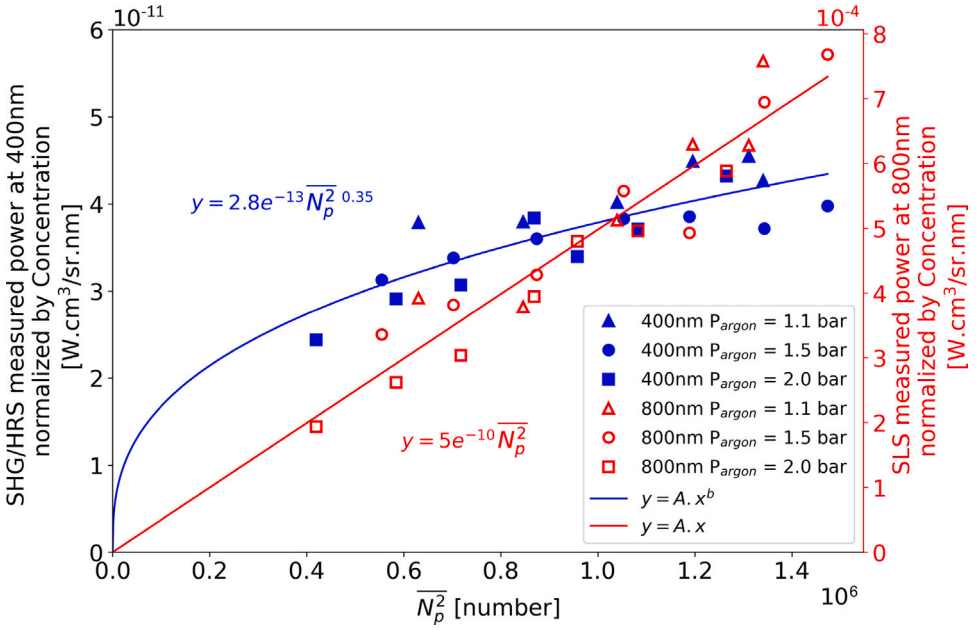

Fig. 8. SHG/HRS signal intensity normalized by the particle concentration for different types of PALAS particles as a function of the square of the number of monomers per aggregate, detected at 35 degrees detection angle and 0.2 mJ pulse energy. The two points with the highest $\overline{N_p^2}$ correspond to the "PALAS" point in the remainder of this study, corresponding to 1.5 bar argon pressure and 1000 Hz electric discharge frequency. (For interpretation of the references to colour in this figure legend, the reader is referred to the web version of this article.)

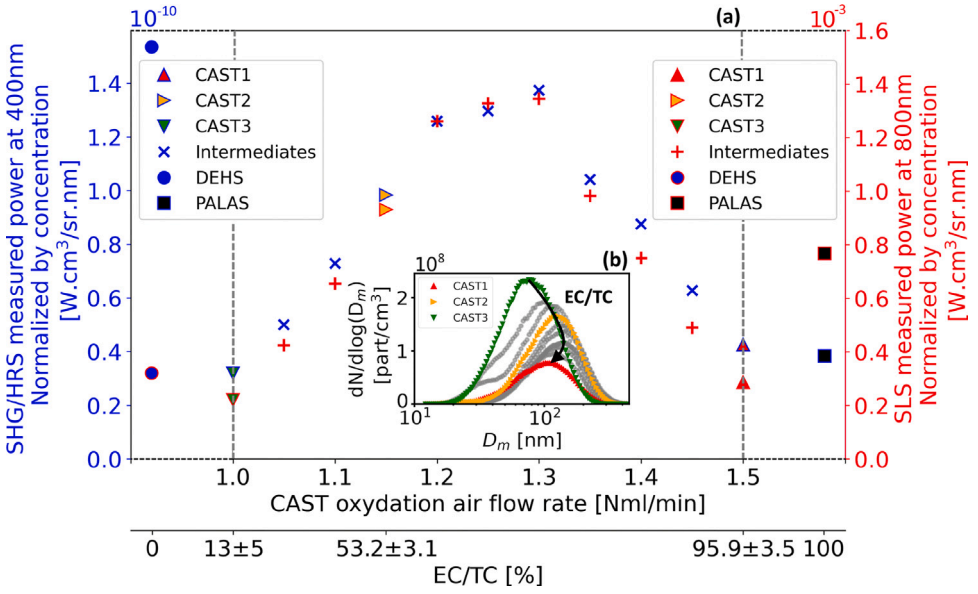

Fig. 9. (a) SHG/HRS and SLS signal intensity normalized by the particle concentration of CAST soot with different quantities of oxidation air, thus giving a different organic content, carried out at 35 degrees detection angle and 0.2 mJ per pulse laser energy. The figure also includes the signal for PALAS particles, being 100% amorphous (without any organic compounds) and DEHS being 100% organic. (b) Particle size distributions measured by SMPS for the different studied operating points, including CAST1, CAST2 and CAST3. The black arrow shows the evolution of the size distribution peaks with increasing EC/TC.

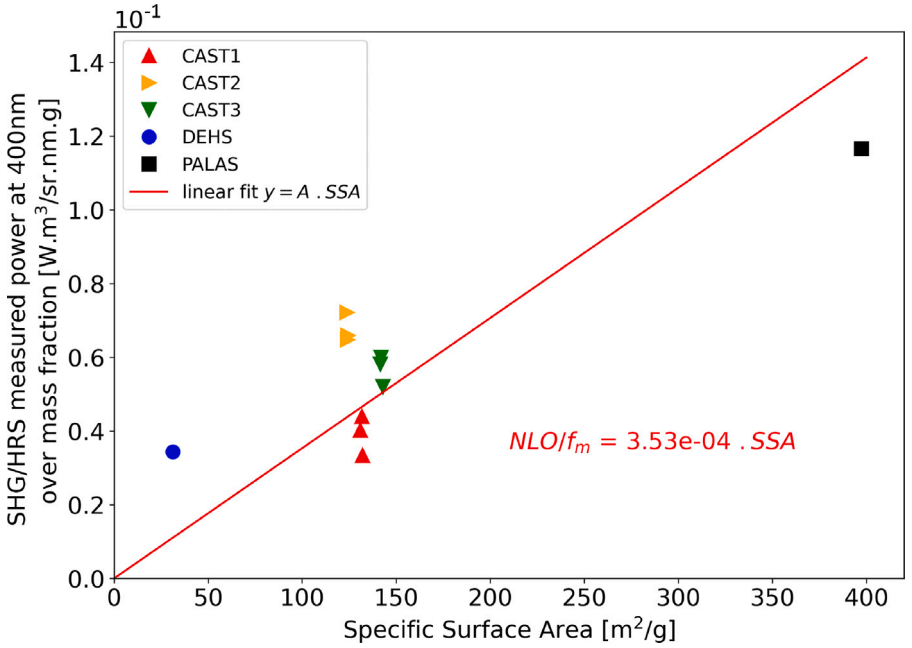

Fig. 10. SHG/HRS signal intensity, normalized by mass fraction, depending on specific surface area, carried out at 35 degrees detection angle and 0.2 mJ per pulse laser energy.

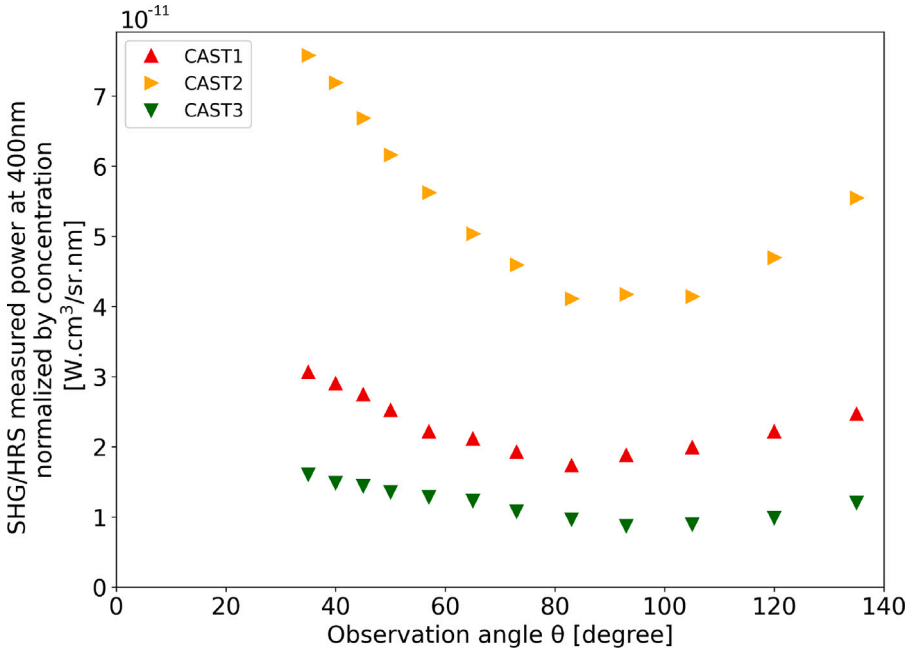

Fig. 11. SHG/HRS signal intensity measured for CAST1, CAST2 and CAST3 at different detection angles and 0.2 mJ per pulse laser energy, normalized by the particle concentration.

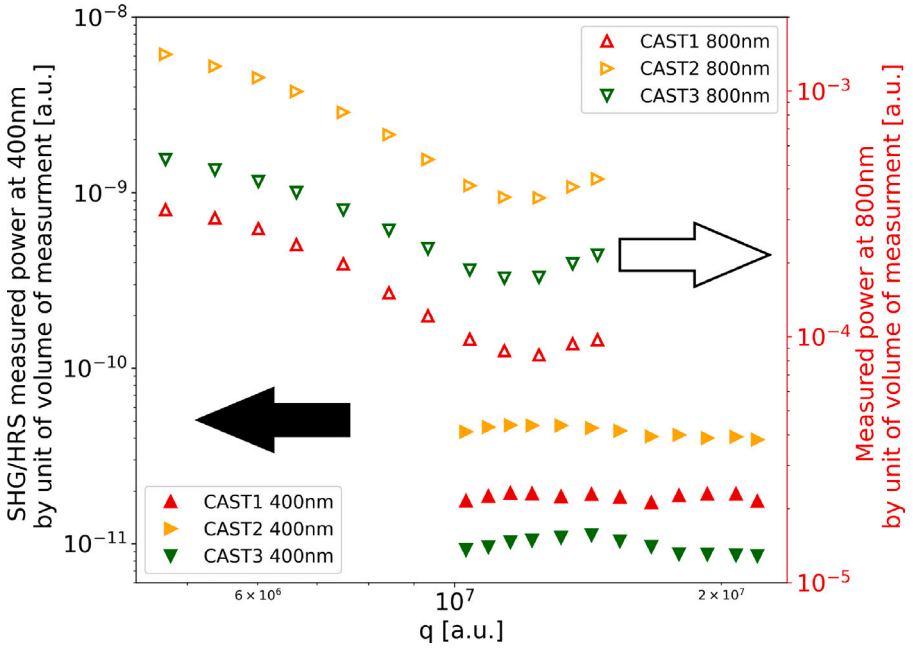

Fig. 12. SHG/HRS and SLS signal intensity measured for CAST1, CAST2 and CAST3 at 35 degrees detection angle and 0.2 mJ per pulse laser energy, normalized by the particle concentration.

following a Guinier and a power law, which is common for linear scattering for fractal aggregates. The SHG/HRS scattering signal on the other hand does not seem to change with q, showing a quite isotropic nature. This isotropic response is typical for incoherent SHG, also named Hyper Rayleigh Scattering (HRS), as explained in Hollis (1988), Das (2006) and in Le Breton (2022). It is a proof that the here observed signal is incoherent, thus associated with HRS.

3.4. Conclusion

The present study allowed to demonstrate the feasibility of an SHG and/or HRS measurement and analysis setup on different types of nanoparticles (black carbon, DEHS droplets, arc generated carbon) in-situ in aerosol phase, which is a novelty compared to previous studies, where SHG was detected either in water solution (Martinez Tomalino, 2009; Martorell et al., 1997; Schürer et al., 2011; Zdanowicz et al., 2013, 2014), or due to SHG sensitive molecules on the surface of aerosols (Qian et al., 2018; Wu et al., 2016). Multiple types of particles were tested, with different size distributions as well as internal structures (organic or graphitic crystalline or amorphous content). By analysing the spectral and temporal response of the aerosol on exposure by femtosecond laser light and by analysing its dependence on the laser power, SHG/HRS can be confirmed for all tested aerosols. Indeed, all aerosols feature a quadratic regime until a certain laser energy, followed by a saturated regime, probably associated with femtosecond laser filamentation. Due to the calibration of the measurements, SHG/HRS could be quantified to the author's knowledge for the first time and is shown to be at least 7 orders of magnitude weaker than linear scattering. Interestingly the size dependence of SHG/HRS is fundamentally different from that of linear scattering. The analysis of the effect of organic content as well as the size of primary spheres of the soot aggregates show that the SHG/HRS signal essentially depends on the aggregate and monomer size, while the fraction of organic or elementary carbon do not seem to have an influence on the signal. One can also see a linear dependence between the SHG/HRS signal and the specific surface area, and it is interesting to stress out the fact, that this linear dependence does not depend on the type of compounds on the surface (elementary or organic carbon). Finally the angular SHG/HRS response of different types of nanoparticles is shown to have a local minimum at around 95 degrees for the three tested aerosols and higher values at the measuring limits at 35 and 135 degrees. A comparison of the angular SHG signal with static light scattering, corrected by the volume of measurement and, in terms of dependence on the scattering wave vector q shows a fundamentally different behaviour, with the linear signal following mostly a power law, while SHG/HRS scattering is found to be isotropic, which suggests that the signal observed in the present work is mainly incoherent. The here observed signal is thus associated with HRS. The results highlight the need of a profound theoretical or model based analysis of the experimental results.

The different results thus show that the here developed experimental setup is suitable and sufficiently sensitive and robust to analyse the NLO response of aerosols. The signals are shown to be proportional to the specific surface area, while the composition does not seem to play a significant role. It would be interesting to complete this experimental study with a theoretical analysis of the presented results and their link with the different processes that happen on the particles' surface. Moreover, an extension of the experiments towards sum frequency generation (SFG, (Boyd, 2008; Brown et al., 2023; Qian et al., 2020a, 2020b)), would allow to

aim at particular molecules and radicals, possibly allowing to develop techniques that are exploitable for the study of atmospheric aerosols including black carbon. In any case, with the linear dependence on particle surface, the here presented setup can give way to a new class of diagnostics, going beyond current in-situ techniques (Michelsen et al., 2015), which are capable of measuring the aerosol's specific surface area and thus help to evaluate the aerosols' toxicity.

CRediT authorship contribution statement

M. Joret: Visualization, Methodology, Investigation, Data curation. **S. Idlahcen:** Writing – review & editing, Validation, Supervision, Methodology, Investigation, Conceptualization. **M. Mazur:** Writing – original draft, Visualization, Supervision, Resources, Project administration, Methodology, Investigation, Funding acquisition, Formal analysis, Data curation, Conceptualization. **J. Yon:** Writing – review & editing, Validation, Supervision, Project administration, Methodology, Investigation, Funding acquisition, Formal analysis, Conceptualization.

Declaration of competing interest

No conflicts of interest exist concerning the present article.

Acknowledgements

The authors acknowledge the funding of M. Joret's PhD by the Normandy region, as well as the experimental equipment by the RENADIAG platform of CORIA, as well as funding from INSA Rouen Normandie. Special thanks also to the technical staff of CORIA laboratory for their support as well as to M. Guillaume le Breton for the fruitful discussions.

Appendix A. Signal calibration

The present section explains the calibration process of the different measurements with the help of the absolutely calibrated integrating sphere described in Section 2.4.

A.1. Calibration of the photo-multiplier measurements

Considering that the photo-multiplier is only measuring the response to one laser pulse (at 100 fs duration) and integrates it over its response time (a few ns), it is possible to express the measured signal as follows :

$$S_m^{PM}\ \Delta t_{PM} = \alpha\ P^{400} \Delta t_{laser} \tag{A.1}$$

with P^{400} the peak power at 400 nm. In order to compare it to the energy emitted during a laser pulse, this value is multiplied by a Δt_{PM}, a time for which the temporal integration of S_m^{PM} would give the same result as the integration of the full temporal profile.

The signal measured from the integrating sphere can be described as:

$$S_{ref}^{PM}\ \cancel{\Delta t_{measure}} = \alpha\ P_{ref}^{400}\ \cancel{\Delta t_{measure}} \tag{A.2}$$

$\Delta t_{measure}$ is the actual time of the measurement since the emission from the integrating sphere is continuous.

Using Eq. (A.2) it is possible to give the expression of the calibration constant α.

$$\alpha = \frac{S_{ref}^{PM}}{P_{ref}^{400}} \tag{A.3}$$

Finally α can be placed in Eq. (A.1) in order to express P^{400} as follows :

$$P^{400} = \frac{S_m^{PM}}{S_{ref}^{PM}} \frac{\Delta t_{PM}}{\Delta t_{laser}}\ P_{ref}^{400} \tag{A.4}$$

It is possible to express P_{ref}^{400} as :

$$P_{ref}^{400} = A_d^{Ang}\ \Delta\Omega_{Ang} \int_\lambda L_\lambda^{ref}\ \tau_\lambda^{400}\ d\lambda \tag{A.5}$$

with $\Delta\Omega_{Ang}$ the solid angle, L_λ^{ref} the radiance of the integrating sphere (known), τ_λ^{400} the transmissivity of the filters installed in front of the PM and A_d the detection surface. The Eq. (A.4) then becomes :

$$P^{400} = \frac{S_m^{PM}}{S_{ref}^{PM}} \frac{\Delta t_{PM}}{\Delta t_{laser}}\ A_d^{Ang}\ \Delta\Omega_{Ang} \int_\lambda L_\lambda^{ref}\ \tau_\lambda^{400}\ d\lambda \tag{A.6}$$

The expression of emission power per solid angle can then be written from Eq. (A.6):

$$\frac{dP^{400}}{d\Omega} = \frac{S_m^{PM}}{S_{ref}^{PM}} \frac{\Delta t_{PM}}{\Delta t_{laser}}\ A_d^{Ang} \int_\lambda L_\lambda^{ref}\ \tau_\lambda^{400}\ d\lambda \tag{A.7}$$

In order to be independent of the spectral transmission width of the filter used at 400 nm, it is possible to express $\frac{P^{400}}{d\Omega}$ by wavelength :

$$\frac{dP^{400}}{d\Omega} = \int_{\lambda} \frac{dP^{400}}{d\Omega}\bigg|_{\lambda} \tau_{\lambda}^{400}\, d\lambda \tag{A.8}$$

Assuming this spectral filter width is small enough to consider $\frac{P^{400}}{d\Omega}\Big|_{\lambda}$ constant over in this range one obtains :

$$\frac{dP^{400}}{d\Omega} = \frac{dP^{400}}{d\Omega}\bigg|_{\lambda} \int_{\lambda} \tau_{\lambda}^{400}\, d\lambda \tag{A.9}$$

The Eq. (A.7) then becomes :

$$\frac{dP^{400}}{d\Omega d\lambda}\bigg|_{\lambda} = \frac{S_m^{PM}}{S_{ref}^{PM}} \frac{\Delta t_{PM}}{\Delta t_{laser}}\, A_d^{Ang}\, \frac{\int_{\lambda} L_{\lambda}^{ref}\, \tau_{\lambda}^{400}\, d\lambda}{\int_{\lambda} \tau_{\lambda}^{400}\, d\lambda} \tag{A.10}$$

A.2. Calibration of the MAYA spectrometer measurements

Unlike the photo-multiplier, the MAYA spectrometer captures spectral emission measurements. These need to be spectrally integrated in order to obtain a value for the signal at 800 nm. The spectral value of the signal S is noted as s_{λ}.

The correction of the profile can then be done wavelength by wavelength :

$$L_{\lambda}^{800} = \frac{L_{\lambda}^{ref}}{s_{\lambda}^{ref}}\, s_{\lambda}^{m} A_d^{Maya} \Delta\Omega^{Maya} \tag{A.11}$$

The collected emission power correspond to the spectral integration of this corrected profile $P_{measured}^{800} = \int_{\lambda} L_{\lambda}^{800}$ and can be expressed in terms of signal as

$$\Delta t_{MAYA}\, P_{measured}^{800} = \int_{\lambda} \frac{s_{\lambda}^{m}}{s_{\lambda}^{ref}}\, L_{\lambda}^{ref} A_d^{Maya} \Delta\Omega^{Maya} d\lambda\, \Delta t_{MAYA} \tag{A.12}$$

$P_{measured}^{800}$ can also be expressed in terms of emission of the aerosol as :

$$\cancel{\Delta t_{MAYA}}\, P_{measured}^{800} = \int_{\lambda} \tau_{\lambda} \frac{dP_{\lambda}^{800}}{d\Omega}\, \Delta\Omega^{Maya} d\lambda\, \Delta t_{Laser}\, f_{laser}\, \cancel{\Delta t_{MAYA}} \tag{A.13}$$

In order to be independent of the spectral width of the peak at 800 nm and assuming the spectral width of the filter is small enough to consider $\frac{dP_{\lambda}^{800}}{d\Omega}$ constant in the wavelength range (which corresponds to a value of P^{800} being equal to the spectral integration of $P_{\lambda}^{800}\Delta\lambda_{800}$) and knowing that the filters employed on this measurement branch are only neutral densities and thus constant in the wavelength range $\tau = \int_{\lambda} \tau_{\lambda} d\lambda$ one obtains :

$$P_{measured}^{800} = \tau\, \frac{dP_{\lambda}^{800}}{d\Omega}\, \Delta\Omega^{Maya} \Delta t_{Laser}\, f_{laser} \tag{A.14}$$

From Eq. (A.13) and by replacing by its expression Eq. (A.12), the expression of the emission power par solid angle becomes :

$$\frac{dP_{\lambda}^{800}}{d\Omega} = \frac{1}{\tau_{\lambda} \cancel{\Delta\Omega^{Maya}}} \int_{\lambda} \frac{s_{\lambda}^{m}}{s_{\lambda}^{ref}}\, L_{\lambda}^{ref} A_d^{Maya} \cancel{\Delta\Omega^{Maya}} d\lambda \frac{1}{\Delta t_{Laser}\, f_{laser}} \tag{A.15}$$

$$\frac{dP_{\lambda}^{800}}{d\Omega} = \frac{A_d^{Maya}}{\tau_{\lambda}\, \Delta t_{Laser}\, f_{laser}} \int_{\lambda} \frac{s_{\lambda}^{m}}{s_{\lambda}^{ref}}\, L_{\lambda}^{ref} d\lambda \tag{A.16}$$

Appendix B. SHG/HRS signal depending on particle volume fraction

Fig. B.13 shows the measured SHG/HRS signal for the different aerosols as a function of the particle volume fraction. The measurements for CAST soot and PALAS follow a linear trend, similar as the dependence of the specific surface area, put forward in Fig. 10. On the other hand, DEHS has a similar level of SHG/HRS, despite its higher volume. While both, specific surface area and the volume fraction increase linearly for aggregates, as shown with the dependence on the number of primary spheres in Fig. 8, the high volume of PALAS does not lead to an increase of SHG/HRS following such a trend. The figure is thus an evidence that the particle volume is not the driving factor for SHG/HRS, but rather the particle surface.

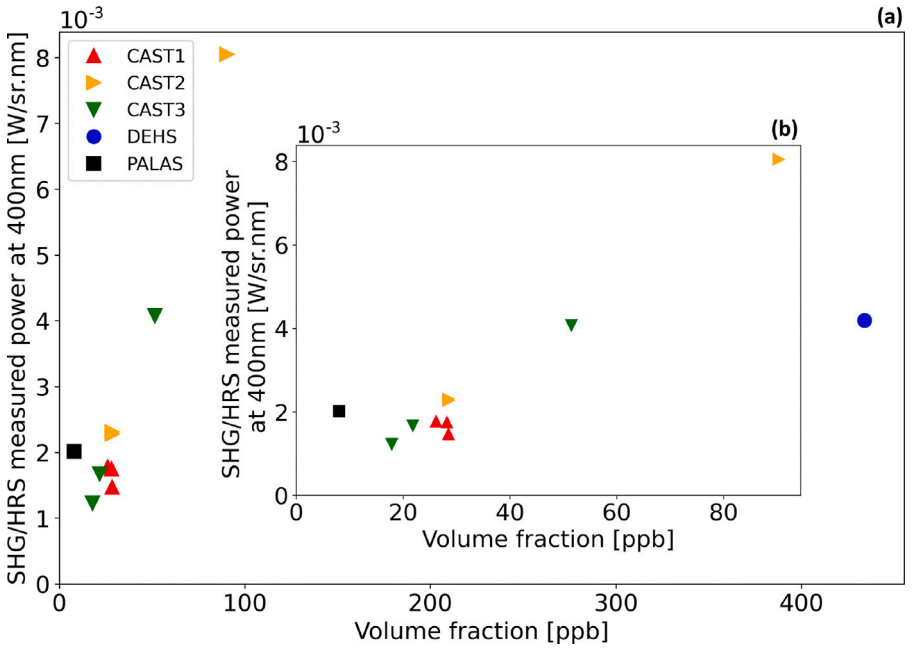

Fig. B.13. (a) SHG/HRS signal intensity depending on the particle volume fraction, measured for CAST1, CAST2, CAST3, PALAS and DEHS at 35 degrees detection angle and 0.2 mJ per pulse laser energy. b) The same signal in the volume fraction range below 100 ppb, thus concentrating on the CAST and PALAS signals.

Data availability

Data will be made available on request.

References

Al Housseiny, H., Singh, M., Emile, S., Nicoleau, M., Wal, R. L. V., & Silveyra, P. (2020). Identification of toxicity parameters associated with combustion produced soot surface chemistry and particle structure by in vitro assays. *Biomedicines*, *8*(9).

Aldén, M., Wallin, S., & Wendt, W. (1984). Applications of two-photon absorption for detection of CO in combustion gases. *Applied Physics B*, *33*(4), 205–208. http://dx.doi.org/10.1007/BF00697329.

Bancelin, S., Aimé, C., Gusachenko, I., Kowalczuk, L., Latour, G., Coradin, T., & Schanne-Klein, M. C. (2015). Second harmonic generation quantitative measurements on collagen fibrils through correlation to electron microscopy. In A. Periasamy, P. T. C. So, & K. König (Eds.), *Multiphoton microscopy in the biomedical sciences XV*. SPIE, http://dx.doi.org/10.1117/12.2077958, URL: https://www.spiedigitallibrary.org/conference-proceedings-of-spie/9329/93292M/Second-harmonic-generation-quantitative-measurements-on-collagen-fibrils-through-correlation/10.1117/12.2077958.short?SSO=1.

Bescond, A. (2015). *Contribution à la métrologie des nanoparticules de suie et à la caractérisation des particules produites par un générateur de référence* (Ph.D. thesis), Saint-Etienne du Rouvray, France: Université de Rouen.

Bescond, A., Yon, J., Ouf, F. X., Ferry, D., Delhaye, D., Gaffié, D., Coppalle, A., & Rozé, C. (2014). Automated determination of aggregate primary particle size distribution by TEM image analysis: Application to soot. *Aerosol Science and Technology*, *48*(8), 831–841. http://dx.doi.org/10.1080/02786826.2014.932896.

Bescond, A., Yon, J., Ouf, F. X., Rozé, C., Coppalle, A., Parent, P., Ferry, D., & Laffon, C. (2016). Soot optical properties determined by analyzing extinction spectra in the visible near-UV: Toward an optical speciation according to constituents and structure. *Journal of Aerosol Science*, *101*, 118–132. http://dx.doi.org/10.1016/j.jaerosci.2016.08.001.

Bonacina, L., Brevet, P. F., Finazzi, M., & Celebrano, M. (2020). Harmonic generation at the nanoscale. *Journal of Applied Physics*, *127*(23), Article 230901. http://dx.doi.org/10.1063/5.0006093, arXiv:https://pubs.aip.org/aip/jap/article-pdf/doi/10.1063/5.0006093/13541867/230901_1_online.pdf.

Bond, T. C., Doherty, S. J., Fahey, D. W., Forster, P. M., Berntsen, T., DeAngelo, B. J., Flanner, M. G., Ghan, S., Kärcher, B., Koch, D., Kinne, S., Kondo, Y., Quinn, P. K., Sarofim, M. C., Schultz, M. G., Schulz, M., Venkataraman, C., Zhang, H., Zhang, S., ... Zender, C. S. (2013). Bounding the role of black carbon in the climate system: A scientific assessment. *Journal of Geophysical Research: Atmospheres*, *118*(11), 5380–5552. http://dx.doi.org/10.1002/jgrd.50171, arXiv:https://agupubs.onlinelibrary.wiley.com/doi/pdf/10.1002/jgrd.50171 URL: https://agupubs.onlinelibrary.wiley.com/doi/abs/10.1002/jgrd.50171.

Bouvier, M., Yon, J., Lefevre, G., & Grisch, F. (2019). A novel approach for in-situ soot size distribution measurement based on spectrally resolved light scattering. *Journal of Quantitative Spectroscopy and Radiative Transfer*, *225*, 58–68. http://dx.doi.org/10.1016/j.jqsrt.2018.12.018, URL: https://www.sciencedirect.com/science/article/pii/S0022407318306496.

Boyd, R. (2008). *Nonlinear optics*. Amsterdam Boston: Academic Press.

Brown, J. B., Qian, Y., Huang-Fu, Z. C., Zhang, T., Wang, H., & Rao, Y. (2023). In situ probing of the surface properties of droplets in the air. *Langmuir*, *39*(31), 10724–10743. http://dx.doi.org/10.1021/acs.langmuir.3c00875, PMID: 37497860.

Cabalín, L., & Laserna, J. (1998). Experimental determination of laser induced breakdown thresholds of metals under nanosecond Q-switched laser operation. *Spectrochimica Acta Part B: Atomic Spectroscopy*, *53*(5), 723–730. http://dx.doi.org/10.1016/S0584-8547(98)00107-4, URL: https://www.sciencedirect.com/science/article/pii/S0584854798001074.

Clark, D. J., Senthilkumar, V., Le, C. T., Weerawarne, D. L., Shim, B., Jang, J. I., Shim, J. H., Cho, J., Sim, Y., Seong, M. J., Rhim, S. H., Freeman, A. J., Chung, K. H., & Kim, Y. S. (2014). Strong optical nonlinearity of CVD-grown MoS_2 monolayer as probed by wavelength-dependent second-harmonic generation. *Physical Review B*, *90*, Article 121409. http://dx.doi.org/10.1103/PhysRevB.90.121409, URL: https://link.aps.org/doi/10.1103/PhysRevB.90.121409.

Das, P. K. (2006). Chemical applications of hyper-Rayleigh scattering in solution. *The Journal of Physical Chemistry B*, *110*(15), 7621–7630. http://dx.doi.org/10.1021/jp0562983, PMID: 16610851.

Das, N. K., Kanclíř, V., Mokrý, P., & Žídek, K. (2021). Bulk and interface second harmonic generation in the Si3N4 thin films deposited via ion beam sputtering. *Journal of Optics*, *23*(2), Article 024003. http://dx.doi.org/10.1088/2040-8986/abe450.

de Beer, A. G. F., Roke, S., & Dadap, J. I. (2011). Theory of optical second-harmonic and sum-frequency scattering from arbitrarily shaped particles. *Journal of the Optical Society of America B (Optical Physics)*, *28*(6), 1374–1384. http://dx.doi.org/10.1364/JOSAB.28.001374, URL: https://opg.optica.org/josab/abstract.cfm?URI=josab-28-6-1374.

Delgado, T., Fortes, F., Cabalín, L., & Laserna, J. (2022). The crucial role of molecular emissions on LIBS differentiation of organic compounds of interest in astrobiology under a mars simulated atmosphere. *Spectrochimica Acta Part B: Atomic Spectroscopy*, *192*, Article 106413. http://dx.doi.org/10.1016/j.sab.2022.106413, URL: https://www.sciencedirect.com/science/article/pii/S058485472200057X.

Durand, M. (2011). *Filamentation laser femtoseconde IR : Interaction de deux filaments et source de rayonnement secondaire longue distance* (Ph.D. thesis), Palaiseau, France: Ecole Polytechnique X.

Ess, M., Ferry, D., Kireeva, E., Niessner, R., Ouf, F. X., & Ivleva, N. (2016). In situ Raman microspectroscopic analysis of soot samples with different organic carbon content: Structural changes during heating. *Carbon*, *105*, 572–585. http://dx.doi.org/10.1016/j.carbon.2016.04.056, URL: https://www.sciencedirect.com/science/article/pii/S0008622316303268.

Geiger, F. M. (2009). Second harmonic generation, sum frequency generation, and $\chi(3)$: Dissecting environmental interfaces with a nonlinear optical swiss army knife. *Annual Review of Physical Chemistry*, *60*(1), 61–83. http://dx.doi.org/10.1146/annurev.physchem.59.032607.093651, URL: https://www.annualreviews.org/doi/10.1146/annurev.physchem.59.032607.093651.

Gonella, G., & Dai, H. L. (2014). Second harmonic light scattering from the surface of colloidal objects: Theory and applications. *Langmuir*, *30*(10), 2588–2599. http://dx.doi.org/10.1021/la403570f, PMID: 24171670.

Highwood, E. J., & Kinnersley, R. P. (2006). When smoke gets in our eyes: The multiple impacts of atmospheric black carbon on climate, air quality and health. *Environment International*, *32*(4), 560–566. http://dx.doi.org/10.1016/j.envint.2005.12.003, URL: https://www.sciencedirect.com/science/article/pii/S0160412005002461.

Hill, W., Lim, E. L., Weeden, C. E., Lee, C., Augustine, M., Chen, K., Kuan, F. C., Marongiu, F., Evans, E. J., Moore, D. A., Rodrigues, F. S., Pich, O., Bakker, B., Cha, H., Myers, R., van Maldegem, F., Boumelha, J., Veeriah, S., Rowan, A., ... Consortium, T. (2023). Lung adenocarcinoma promotion by air pollutants. *Nature*, *616*(7955), 159–167. http://dx.doi.org/10.1038/s41586-023-05874-3.

Hollis, D. B. (1988). Review of hyper-Rayleigh and second-harmonic scattering in minerals and other inorganic solids. *American Mineralogist*, *73*(7–8), 701–706, arXiv:https://pubs.geoscienceworld.org/msa/ammin/article-pdf/73/7-8/701/4221440/am73_701.pdf.

Jacobson, M. Z. (2010). Short-term effects of controlling fossil-fuel soot, biofuel soot and gases, and methane on climate, arctic ice, and air pollution health. *Journal of Geophysical Research: Atmospheres*, *115*(D14), http://dx.doi.org/10.1029/2009JD013795, arXiv:https://agupubs.onlinelibrary.wiley.com/doi/pdf/10.1029/2009JD013795 URL: https://agupubs.onlinelibrary.wiley.com/doi/abs/10.1029/2009JD013795.

Juarez-Facio, A. T., Castilla, C., Corbière, C., Lavanant, H., Afonso, C., Morin, C., Merlet-Machour, N., Chevalier, L., Vaugeois, J. M., Yon, J., & Monteil, C. (2022). Development of a standardized in vitro approach to evaluate microphysical, chemical, and toxicological properties of combustion-derived fine and ultrafine particles. *Journal of Environmental Sciences*, *113*, 104–117. http://dx.doi.org/10.1016/j.jes.2021.06.001, URL: https://www.sciencedirect.com/science/article/pii/S1001074221002291.

Knauer, M., Schuster, M. E., Su, D., Schlögl, R., Niessner, R., & Ivleva, N. P. (2009). Soot structure and reactivity analysis by Raman microspectroscopy, temperature-programmed oxidation, and high-resolution transmission electron microscopy. *The Journal of Physical Chemistry A*, *113*(50), 13871–13880. http://dx.doi.org/10.1021/jp905639d, PMID: 19899796.

Le Breton, G. (2022). *Second harmonic generation of non-resonant liquid : from the molecular response to the experimental measurement* (Ph.D. thesis), (2022LYO10015), Université Claude Bernard - Lyon I, URL: https://theses.hal.science/tel-04022967.

Makarov, S. V., Petrov, M. I., Zywietz, U., Milichko, V., Zuev, D., Lopanitsyna, N., Kuksin, A., Mukhin, I., Zograf, G., Ubyivovk, E., Smirnova, D. A., Starikov, S., Chichkov, B. N., & Kivshar, Y. S. (2017). Efficient second-harmonic generation in nanocrystalline silicon nanoparticles. *Nano Letters*, *17*(5), 3047–3053. http://dx.doi.org/10.1021/acs.nanolett.7b00392, PMID: 28409641.

Malcom Brown, R., Jr., Millard, A. C., & Campagnola, P. J. (2003). Macromolecular structure of cellulose studied by second-harmonic generation imaging microscopy. *Optics Letters*, *28*(22), 2207–2209. http://dx.doi.org/10.1364/OL.28.002207, URL: https://www.osapublishing.org/ol/abstract.cfm?uri=ol-28-22-2207.

Marinescu, M. (2019). Synthesis and nonlinear optical studies on organic compounds in laser-deposited films. In *Applied surface science*. IntechOpen, http://dx.doi.org/10.5772/intechopen.83234, URL: https://www.intechopen.com/books/applied-surface-science/synthesis-and-nonlinear-optical-studies-on-organic-compounds-in-laser-deposited-films.

Martinez Tomalino, L. O. (2009). *Anwendung der optischen Frequenz- Verdopplung in der Partikelmesstechnik* (Ph.D. thesis), Erlangen, Germany: Friedrich-Alexander-Universität Erlangen-Nürnberg.

Martorell, J., Vilaseca, R., & Corbalán, R. (1997). Scattering of second-harmonic light from small spherical particles ordered in a crystalline lattice. *Physical Review A*, *55*, 4520–4525. http://dx.doi.org/10.1103/PhysRevA.55.4520, URL: https://link.aps.org/doi/10.1103/PhysRevA.55.4520.

Matrokhin, A. A., Shevchenko, M. A., Umanskaya, S. F., Tareeva, M. V., Kudryavtseva, A. D., & Tcherniega, N. V. (2022). Second-harmonic generation in aggregates of lithium niobate particles formed upon suspension freezing. *Photonics*, *9*(10), http://dx.doi.org/10.3390/photonics9100705, URL: https://www.mdpi.com/2304-6732/9/10/705.

Michelsen, H. (2017). Probing soot formation, chemical and physical evolution, and oxidation: A review of in situ diagnostic techniques and needs. *Proceedings of the Combustion Institute*, *36*(1), 717–735. http://dx.doi.org/10.1016/j.proci.2016.08.027, URL: https://www.sciencedirect.com/science/article/pii/S1540748916304163.

Michelsen, H., Schulz, C., Smallwood, G., & Will, S. (2015). Laser-induced incandescence: Particulate diagnostics for combustion, atmospheric, and industrial applications. *Progress in Energy and Combustion Science*, *51*, 2–48. http://dx.doi.org/10.1016/j.pecs.2015.07.001, URL: https://www.sciencedirect.com/science/article/pii/S0360128515300071.

Ouf, F. X., Bourrous, S., Vallières, C., Yon, J., & Lintis, L. (2019). Specific surface area of combustion emitted particles: Impact of primary particle diameter and organic content. *Journal of Aerosol Science*, *137*, Article 105436. http://dx.doi.org/10.1016/j.jaerosci.2019.105436, URL: https://www.sciencedirect.com/science/article/pii/S0021850219305324.

Ouf, F. X., Parent, P., Laffon, C., Marhaba, I., Ferry, D., Marcillaud, B., Antonsson, E., Benkoula, S., Liu, X. J., Nicolas, C., Robert, E., Patanen, M., Barreda, F. A., Sublemontier, O., Coppalle, A., Yon, J., Miserque, F., Mostefaoui, T., Regier, T. Z., ... Miron, C. (2016). First in-flight synchrotron X-ray absorption and photoemission study of carbon soot nanoparticles. *Scientific Reports*, *6*(1), 36495. http://dx.doi.org/10.1038/srep36495.

Paul, H. J., & Corn, R. M. (1997). Second-harmonic generation measurements of electrostatic biopolymer-surfactant coadsorption at the water/1,2-dichloroethane interface. *The Journal of Physical Chemistry B*, *101*(23), 4494–4497. http://dx.doi.org/10.1021/jp970751w.

Qian, Y., Brown, J. B., Huang-Fu, Z. C., Zhang, T., Wang, H., Wang, S., Dadap, J. I., & Rao, Y. (2022). In situ analysis of the bulk and surface chemical compositions of organic aerosol particles. *Communications Chemistry*, *5*(1), 58. http://dx.doi.org/10.1038/s42004-022-00674-8.

Qian, Y., Brown, J. B., Zhang, T., Huang-Fu, Z. C., & Rao, Y. (2022). In situ detection of chemical compositions at nanodroplet surfaces and in-nanodroplet phases. *The Journal of Physical Chemistry A*, *126*(23), 3758–3764. http://dx.doi.org/10.1021/acs.jpca.2c03346, PMID: 35667005.

Qian, Y., Deng, G. h., Lapp, J., & Rao, Y. (2019). Interfaces of gas–aerosol particles: Relative humidity and salt concentration effects. *The Journal of Physical Chemistry A*, *123*(29), 6304–6312. http://dx.doi.org/10.1021/acs.jpca.9b03896, PMID: 31253043.

Qian, Y., Deng, G. h., & Rao, Y. (2018). In situ chemical analysis of the gas–aerosol particle interface. *Analytical Chemistry*, *90*(18), 10967–10973. http://dx.doi.org/10.1021/acs.analchem.8b02537.

Qian, Y., Deng, G. h., & Rao, Y. (2020a). In situ spectroscopic probing of polarity and molecular configuration at aerosol particle surfaces. *The Journal of Physical Chemistry Letters*, *11*(16), 6763–6771. http://dx.doi.org/10.1021/acs.jpclett.0c02013, PMID: 32787224.

Qian, Y., Deng, G. h., & Rao, Y. (2020b). In situ spectroscopic probing of polarity and molecular configuration at aerosol particle surfaces. *The Journal of Physical Chemistry Letters*, *11*(16), 6763–6771. http://dx.doi.org/10.1021/acs.jpclett.0c02013, PMID: 32787224.

Rice, W. L., Firdous, S., Gupta, S., Hunter, M., Foo, C. W. P., Wang, Y., Kim, H. J., Kaplan, D. L., & Georgakoudi, I. (2008). Non-invasive characterization of structure and morphology of silk fibroin biomaterials using non-linear microscopy. *Biomaterials*, *29*(13), 2015–2024. http://dx.doi.org/10.1016/j.biomaterials.2007.12.049, URL: http://www.sciencedirect.com/science/article/pii/S0142961207010630.

Roke, S., & Gonella, G. (2012). Nonlinear light scattering and spectroscopy of particles and droplets in liquids. *Annual Review of Physical Chemistry*, *63*, 353–378. http://dx.doi.org/10.1146/annurev-physchem-032511-143748, URL: https://www.annualreviews.org/content/journals/10.1146/annurev-physchem-032511-143748.

Schneider, L., Schmid, H. J., & Peukert, W. (2007). Influence of particle size and concentration on the second-harmonic signal generated at colloidal surfaces. *Applied Physics B*, *87*(2), 333–339. http://dx.doi.org/10.1007/s00340-007-2597-7.

Schürer, B., Hoffmann, M., Wunderlich, S., Harnau, L., Peschel, U., Ballauff, M., & Peukert, W. (2011). Second harmonic light scattering from spherical polyelectrolyte brushes. *The Journal of Physical Chemistry C*, *115*(37), 18302–18309. http://dx.doi.org/10.1021/jp2064547.

Sirven, J. B., Mauchien, P., & Sallé, B. (2008). Analytical optimization of some parameters of a laser-induced breakdown spectroscopy experiment. *Spectrochimica Acta Part B: Atomic Spectroscopy*, *63*(10), 1077–1084. http://dx.doi.org/10.1016/j.sab.2008.08.013, URL: https://www.sciencedirect.com/science/article/pii/S0584854708002498. A collection of papers presented at the Euro Mediterranean Symposium on Laser Induced Breakdown Spectroscopy (EMSLIBS 2007).

Son, E. E., & Tereshonok, D. V. (2010). Thermal and plasma flow control. *Physica Scripta*, *2010*(T142), Article 014039. http://dx.doi.org/10.1088/0031-8949/2010/T142/014039.

Sorensen, C. M. (2001). Light scattering by fractal aggregates: A review. *Aerosol Science and Technology*, *35*(2), 648–687. http://dx.doi.org/10.1080/02786820117868, arXiv:https://www.tandfonline.com/doi/pdf/10.1080/02786820117868 URL: https://www.tandfonline.com/doi/abs/10.1080/02786820117868.

Stoller, P., Reiser, K. M., Celliers, P. M., & Rubenchik, A. M. (2002). Polarization-modulated second harmonic generation in collagen. *Biophysical Journal*, *82*(6), 3330–3342. http://dx.doi.org/10.1016/S0006-3495(02)75673-7, URL: http://www.sciencedirect.com/science/article/pii/S0006349502756737.

Vielreicher, M., Schürmann, S., Detsch, R., Schmidt, M. A., Buttgereit, A., Boccaccini, A., & Friedrich, O. (2013). Taking a deep look: modern microscopy technologies to optimize the design and functionality of biocompatible scaffolds for tissue engineering in regenerative medicine. *Journal of the Royal Society Interface*, *10*(86), Article 20130263. http://dx.doi.org/10.1098/rsif.2013.0263, URL: https://royalsocietypublishing.org/doi/full/10.1098/rsif.2013.0263.

von Bismarck-Osten, C., Birmili, W., Ketzel, M., Massling, A., Petäjä, T., & Weber, S. (2013). Characterization of parameters influencing the spatio-temporal variability of urban particle number size distributions in four European cities. *Atmospheric Environment*, *77*, 415–429. http://dx.doi.org/10.1016/j.atmosenv.2013.05.029, URL: https://www.sciencedirect.com/science/article/pii/S1352231013003725.

von der Linde, D., Sokolowski-Tinten, K., & Bialkowski, J. (1997). Laser–solid interaction in the femtosecond time regime. *Applied Surface Science*, *109–110*, 1–10. http://dx.doi.org/10.1016/S0169-4332(96)00611-3, URL: https://www.sciencedirect.com/science/article/pii/S0169433296006113.

Wan, E., Sun, Z., & Liu, Y. (2021). Real-time in situ detection and source tracing of different soot. *Optik*, *245*, Article 167711. http://dx.doi.org/10.1016/j.ijleo.2021.167711, URL: https://www.sciencedirect.com/science/article/pii/S0030402621013085.

Wang, H., Yan, E., Borguet, E., & Eisenthal, K. (1996). Second harmonic generation from the surface of centrosymmetric particles in bulk solution. *Chemical Physics Letters*, *259*(1), 15–20. http://dx.doi.org/10.1016/0009-2614(96)00707-5, URL: https://www.sciencedirect.com/science/article/pii/0009261496007075.

Wu, Y., Li, W., Xu, B., Li, X., Wang, H., McNeill, V. F., Rao, Y., & Dai, H. L. (2016). Observation of organic molecules at the aerosol surface. *The Journal of Physical Chemistry Letters*, *7*(12), 2294–2297. http://dx.doi.org/10.1021/acs.jpclett.6b00872.

Wunderlich, S., Zhuromskyy, O., Schürer, B., Haderlein, M., Sauerbeck, C., Peukert, W., & Peschel, U. (2012). Second harmonic generation from metallic and dielectric spherical nanoparticles. In *Conference on lasers and electro-optics 2012* (p. QTu1F.4). Optica Publishing Group, http://dx.doi.org/10.1364/QELS.2012.QTu1F.4, URL: https://opg.optica.org/abstract.cfm?URI=QELS-2012-QTu1F.4,

Yon, J., Bescond, A., & Ouf, F. X. (2015). A simple semi-empirical model for effective density measurements of fractal aggregates. *Journal of Aerosol Science*, *87*, 28–37. http://dx.doi.org/10.1016/j.jaerosci.2015.05.003, URL: https://www.sciencedirect.com/science/article/pii/S0021850215000701.

Zang, H., Fu, Y., Hou, M., Li, H., Yamanouchi, K., & Xu, H. (2020). Ultrafast swelling and shrinking of soot in alkanol–air flames induced by femtosecond laser filamentation. *Combustion and Flame*, *212*, 345–351. http://dx.doi.org/10.1016/j.combustflame.2019.11.009, URL: http://www.sciencedirect.com/science/article/pii/S0010218019305140.

Zang, H. W., Li, H. L., Su, Y., Fu, Y., Hou, M. Y., Baltuška, A., Yamanouchi, K., & Xu, H. (2018). Third-harmonic generation and scattering in combustion flames using a femtosecond laser filament. *Optics Letters*, *43*(3), 615–618. http://dx.doi.org/10.1364/OL.43.000615, URL: https://www.osapublishing.org/ol/abstract.cfm?uri=ol-43-3-615.

Zdanowicz, M., Harra, J., Mäkelä, J. M., Heinonen, E., Ning, T., Kauranen, M., & Genty, G. (2013). Ordered multilayer silica-metal nanocomposites for second-order nonlinear optics. *Applied Physics Letters*, *103*(25), Article 251907. http://dx.doi.org/10.1063/1.4852795.

Zdanowicz, M., Harra, J., Mäkelä, J. M., Heinonen, E., Ning, T., Kauranen, M., & Genty, G. (2014). Second-harmonic response of multilayer nanocomposites of silver-decorated nanoparticles and silica. *Scientific Reports*, *4*(1), http://dx.doi.org/10.1038/srep05745.